INTERNATIONAL JOURNAL FOR NUMERICAL METHODS IN FLUIDS
Int. J. Numer. Meth. Fluids 2007; **53**:629–650
Published online 24 July 2006 in Wiley InterScience (www.interscience.wiley.com). DOI: 10.1002/fld.1299

An application of the finite difference-based lattice Boltzmann model to simulating flow-induced noise

Hokeun Kang[1,*,†] and Michihisa Tsutahara[2]

[1]*Institute of Marine Industry, Gyeongsang National University, Korea*
[2]*Graduate School of Science and Technology, Kobe University, Japan*

SUMMARY

This paper presents a novel approach to simulate aerodynamically generated sounds by modifying the finite difference-based lattice BGK compressible fluid model for the purpose of speeding up the calculation and also stabilizing the numerical scheme. With the model, aerodynamic sounds generated by a uniform flow around a two-dimensional circular cylinder at $Re = 150$ are simulated. The third-order-accurate up-wind scheme is used for the spatial derivatives, and the second-order-accurate Runge–Kutta method is applied for the time marching. The results show that we successively capture very small acoustic pressure fluctuations, with the same frequency of the Karman vortex street, much smaller than the whole pressure fluctuation around a circular cylinder. The propagation velocity of the acoustic waves shows that the points of peak pressure are biased upstream owing to the Doppler effect in the uniform flow. For the downstream, on the other hand, it is faster. It is also apparent that the amplitude of sound pressure is proportional to $r^{-1/2}$, r being the distance from the centre of the circular cylinder. Moreover, the edgetone generated by a two-dimensional jet impinging on a wedge to predict the frequency characteristics of the discrete oscillations of a jet-edge feedback cycle is investigated. The jet is chosen long enough to guarantee the parabolic velocity profile of the jet at the outlet, and the edge is of an angle of $\alpha = 23°$. At a stand-off distance w, the edge is inserted along the centreline of the jet, and a sinuous instability wave with real frequency is assumed to be created in the vicinity of the nozzle exit and to propagate towards the downstream. We have succeeded in capturing small pressure fluctuations resulting from periodic oscillation of jet around the edge. Copyright © 2006 John Wiley & Sons, Ltd.

Received 20 February 2006; Revised 17 May 2006; Accepted 19 May 2006

KEY WORDS: finite difference-based lattice Boltzmann method (FDLBM); compressible fluid; aerodynamic sound; edgetone; feedback

*Correspondence to: Hokeun Kang, Institute of Marine Industry, Gyeongsang National University, 445 Inpyeong-dong, Tongyeong, Gyeongnam 650-160, Republic of Korea.
†E-mail: kanghokeun@chol.com

Contract/grant sponsor: Korea Research Foundation Grant; contract/grant number: KRF-2005-050-D00002

1. INTRODUCTION

Works in the field of computational aeroacoustics have been developed via direct simulation by applying a large amount of calculation resources. Especially, with the increase of speed of transport vehicles like airplane, automobiles, and trains in recent years, flow noise has become a large environmental problem. There are two kinds of noise: vibration noise created by the vibration of object, and aerodynamic noise produced by the unsteady motion of fluid. The energy of sound due to the object vibration is proportional to $O(10^{-2})$ of the momentum energy $\rho u^2/2$ while the aerodynamic noise is proportional to $O(10^{-5}$–$10^{-8})$. Understanding the aerodynamic noise by analysing its mechanism is therefore difficult. In the numerical research of the aerodynamic sound, it can be possible to analyse the information of the detailed flow field, which is not obtained in the experiments, by directly solving the compressible Navier–Stokes equation. However, in studying the aerodynamic sound by the numerical method, a number of things are necessary: a highly accurate scheme to realize the sound pressure ($O(10^{-4})$) against the static pressure; a wide calculation area to obtain far away sound pressure field; and removal of the numerical reflection at the boundary.

The flow around a circular cylinder [1, 2] or an airfoil [3] has been studied experimentally and numerically for quite a while because it is one of the abundant phenomena of the fundamental fluid mechanics. Yet, in spite of its simplicity, a lot of unsolved problems still exist. One of them is the generation mechanism of acoustic waves by the flow around the cylinder. This has also been studied experimentally and numerically to some extent. The numerical analyses has been done in the conventional way that a vorticity dominant near field is simulated first and then an acoustic far field is obtained using approximated equations derived from the acoustic analogy [4]. So far most of the computational work on the sound generation due to flow past a circular cylinder has been done using the hybrid method [5], acoustic/viscous splitting methods [6, 7] and the direct numerical simulation (DNS) [8, 9]. Furthermore, in the edgetone, a discrete frequency sound is produced by several flow geometries in which a free shear layer interacts with a solid boundary. One well-known device which produces discrete frequency sound in this way is the edge tone. Its sound is generated because the impinging jet forms a self-excited flow maintained by a feedback loop. Particularly obvious are the main features by the simplifying considerations first stated by Powell [10, 11]. This edgetone is an effective device for transforming the energy of the jet into acoustic radiation at a discrete frequency, and it is used as the source, which is coupled to a resonator in several wind instruments. Since the last century the edgetone has been the subject of a large number of both experimental and theoretical investigations. Some books and reviews on edgetones are found in this fields [12–14]. In his experimental investigation, Brown [12] encompasses four stages of edgetone and shows that an alternating vortex street is formed in the jet. Holger *et al*. [13] examined the jet-edge interaction mechanism by considering a flat plate place with a fully developed vortex street, and Crighton [14] performed to a linear analysis to predict the frequency characteristics of the feedback cycle. Moreover, two-dimensional numerical simulation on an edgetone and the associated self-sustained flows were reported by Ohring [15], Benard [16] and Park and Lee [17]. However, in the fields stated above, the studies applying the lattice Boltzmann method are recently developed by Buick *et al*. [18] and Tsutahara *et al*. [19].

In the present work we propose a modified model using the lattice BGK 21-velocity compressible fluid model in FDLBM to speed up the calculation and also to stabilize the numerical scheme through a simple shock tube problem. With the model, we simulate the generation and propagation mechanism of the acoustic waves produced by a turbulent wake of a circular cylinder in a uniform

DOI: 10.1002/fld

flow at low Reynolds number. The predicted sound spectra with the vortex/flow dynamics are clarified and the effect of the Mach number using the sound velocity is also examined. To examine the characteristic of the lattice dependence, we also investigate 2D computations of the tone noise radiated by an airfoil (NACA0012) with a blunt trailing edge at high incidence and low Reynolds number. Finally, we extend our model to the onset issue for an edge tone generated by a two-dimensional jet impinging on a wedge to predict the frequency characteristics of the discrete oscillations of a jet-edge feedback cycle. As a result, the model can be easily used to simulate a complex fluid flows and associated transport phenomena including a shock-capturing and aeroacoustics.

2. COMPUTATIONAL METHODOLOGY

Developed from the lattice gas automata (LGA or lattice gas cellular automaton, LGCA) model [20], the lattice Boltmzan method (LBM) [21–23] is a quite recent approach for simulating fluid flow, which has been proven to be a valid and efficient tool in a variety of complex flow problems. Considered an attractive alternative to conventional finite-difference schemes because it recovers the Navier–Stokes equations, the lattice Boltzmann method is computationally more stable, and easily parallelizable. In traditional numerical methods, the macroscopic variables are obtained by solving the Navier–Stokes equations. But the LBM solves the microscopic kinetic equation for particle distribution function from which the particles move at unit speed on a regular grid subject to particle movement and simplified collision rules which conserve the total fluid mass, momentum and energy. The presently popular method uses regularly spaced lattices and cannot handle curved boundaries with desirable flexibility. To circumvent such difficulties, the finite difference-based lattice Boltzmann method (FDLBM) [24, 25] in curvilinear coordinates is explored using body-fitted coordinates with nonuniform grids [26]. The method makes it possible and easy to simulate the complicated object shapes, and the application to various flow fields is attained. This method has high flexibility for coordinate system selection and is often the choice among various schemes.

The Boltzmann equation governing the velocity distribution function f_i may be written, with a single relaxation time ϕ, as

$$\frac{\partial f_i}{\partial t} + \mathbf{c}_i \cdot \nabla f_i = -\frac{1}{\phi}(f_i - f_i^{\mathrm{eq}}) \tag{1}$$

Here, the real number f_i is the normalized number of particles at each lattice node and time t, moving in direction i. The microscopic dynamics associated with Equation (1) can be viewed as a two-step process of movement and collision. In the collision step, the distribution functions at each site relax toward a state of local equilibrium. The form of RHS term, given in Equation (1), represents a relaxation of the distribution towards its equilibrium value and recovers the nonlinear form of the fluid, ensuring that the fully nonlinear Navier–Stokes equation is satisfied. The equilibrium distribution functions f_i^{eq} depend on the fluid density ρ, velocity $\mathbf{u}$, and internal energy e, at each site which can be calculated from the distribution functions as

$$\rho = \sum_i f_i \tag{2}$$

$$\rho \mathbf{u} = \sum_i \mathbf{c}_i f_i \tag{3}$$

DOI: 10.1002/fld

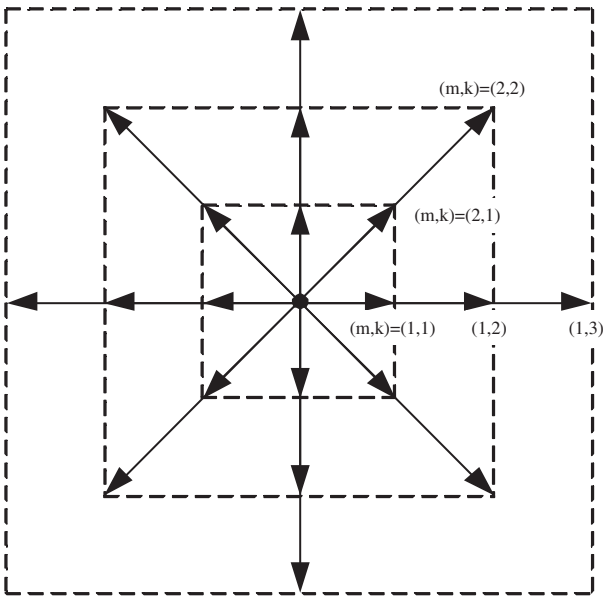

Figure 1. A compressible lattice Boltzmann model (D2Q21). The index $m=1$ indicates the particle which moves in the orthogonal direction and $m=2$ indicates the particle which moves in the diagonal direction. The k represents the speed of particle which moves in the nearest neighbouring lattice.

and

$$\rho e = \sum_i \frac{1}{2} c^2 f_i - \frac{1}{2} \rho u^2 \tag{4}$$

Up to $O(u^3)$, we assume that the equilibrium distribution function is expressed as

$$f_i^{\mathrm{eq}} = F_i \rho \left[1 - 2Bc_{i\alpha}u_\alpha + 2B^2(c_{i\alpha}u_\alpha) + Bu^2 - \tfrac{4}{3}B^3(c_{i\alpha}u_\alpha) - 2B^2 c_{i\alpha}u_\alpha u^2 \right] \tag{5}$$

where the Greek subscripts represent vector components. The moving particles are allowed to move with five kinds of speed, c, $2c$, $3c$, $\sqrt{2}c$, and $2\sqrt{2}c$, and the particles are 21 kinds, as shown in Figure 1. The functions F_i and B, respectively, are determined by

$$F_1 = 1 + \frac{5}{4Bc^2}\left(\frac{17}{96B^2c^4} + \frac{35}{48Bc^2} + \frac{49}{45} \right) \tag{6}$$

$$F_{2\text{–}5} = -\frac{1}{8Bc^2}\left(\frac{13}{16B^2c^4} + \frac{71}{24Bc^2} + 3 \right) \tag{7}$$

$$F_{6\text{–}9} = \frac{1}{16Bc^2}\left(\frac{5}{16B^2c^4} + \frac{25}{24Bc^2} + \frac{3}{5} \right) \tag{8}$$

DOI: 10.1002/fld

$$F_{10\text{–}13} = -\frac{1}{24Bc^2}\left(\frac{1}{16B^2c^4} + \frac{1}{8Bc^2} + \frac{1}{15}\right) \tag{9}$$

$$F_{14\text{–}17} = \frac{1}{4B^3c^6}\left(\frac{Bc^2}{3} + \frac{1}{8}\right) \tag{10}$$

$$F_{18\text{–}21} = -\frac{1}{153B^3c^6}(2Bc^2 + 3) \tag{11}$$

$$B = -\frac{1}{2e} \tag{12}$$

The models for compressible fluids are sometimes unstable in calculation. However, by using the finite difference, it stabilizes the calculation considerably. For this purpose, this paper employs the discretized BGK equation (1). This equation is shown to lead the Navier–Stokes equations by the Chapman–Enskog expansion, and the term $(\phi - 1/2)$ in transfer coefficient changes into ϕ. The relationship between the kinematic viscosity and relaxation time factor becomes

$$v = \frac{2}{D}\rho e\phi \tag{13}$$

Here, D is the characteristic dimension and the value of D is 2 for two-dimensional case. For high Reynolds number flows which are important in engineering fields, $v \ll 1$ must be satisfied. If Euler's first-order forward difference scheme is used for time integral, the equation is transformed as

$$f_i^{n+1} = f_i^n + \Delta t\left[-c_{i\alpha}\frac{\partial f_i^n}{\partial x_\alpha} - \frac{1}{\phi}(f_i^n - f_i^{\mathrm{eq}})\right] \tag{14}$$

where Δt is the time increment. In Equation (14), the condition of stability for the collision term must be satisfied $\Delta t/\phi < 2.0$, which states that the distribution function approaches its equilibrium state by every collision. Relations between v and $\Delta t/\phi$ lead that, for high Reynolds number flows, the time increment chosen must be small and the calculation time will be very long. Therefore, an equation in which the third term is added to the discretized BGK equation (Equation (1)) is transformed

$$\frac{\partial f_i}{\partial t} + c_{i\alpha}\frac{\partial f_i}{\partial x_\alpha} - Ac_{i\alpha}\frac{\partial}{\partial x_\alpha}\left(\frac{f_i - f_i^{\mathrm{eq}}}{\phi}\right) = -\frac{1}{\phi}(f_i - f_i^{\mathrm{eq}}) \tag{15}$$

where $A(>0)$ is a constant. Then the relationship is changed as follows:

$$v = \frac{2}{D}\rho e(\phi - A) \tag{16}$$

By conducting such conversion, it is possible to modify the relationship between the coefficient of the kinematic viscosity and the single relaxation coefficient $\phi \sim v$ to $\phi \to A \sim v$ in FDLBM. Therefore, the single relaxation coefficient ϕ becomes $\phi \to \phi - A$ in the flow of high Reynolds number, and the transformed model of FDLBM makes it possible to calculate with the fixed value of ϕ which is taken in high Reynolds number flows. Furthermore, it becomes possible that the

DOI: 10.1002/fld

calculation of Δt can easily or stably simulate up to large value, while $\Delta t/\phi = 2.0$ is an upper limit for the collision term in the conventional FDLBM model.

The macroscopic equations can be derived from the lattice Boltzmann equations by conducting multi-scale expansions in the time and space derivatives such that

$$\frac{\partial}{\partial t} \to \varepsilon \frac{\partial}{\partial t_1} + \varepsilon^2 \frac{\partial}{\partial t_2} \tag{17}$$

$$\frac{\partial}{\partial x_\alpha} \to \varepsilon \frac{\partial}{\partial x_{1\alpha}} \tag{18}$$

and the distribution function is expanded in powers of ε as

$$f_i = f_i^{\mathrm{eq}} + \varepsilon f_i^{(1)} + \varepsilon^2 f_i^{(2)} + \cdots \tag{19}$$

where ε is the Knudsen number which must be small. Substituting the expression for the equilibrium distribution functions of Equation (5), the Chapman–Enskog expansions of Equations (17)–(19), the Navier–Stokes equations are obtained as

$$\frac{\partial \rho}{\partial t} + \frac{\partial \rho u_\alpha}{\partial x_{1\alpha}} = 0 \tag{20}$$

$$\frac{\partial \rho u_\alpha}{\partial t} + \frac{\partial \rho u_\alpha u_\beta}{\partial x_\beta} = -\frac{\partial p}{\partial x_\alpha} + \frac{\partial}{\partial x_\beta} \mu \left(\frac{\partial u_\alpha}{\partial x_\beta} + \frac{\partial u_\beta}{\partial x_\alpha} \right) + \frac{\partial}{\partial x_\alpha} \left(\lambda \frac{\partial u_\beta}{\partial x_\beta} \right) \tag{21}$$

$$\begin{aligned} &\frac{\partial}{\partial t} \rho \left(\frac{1}{2} u^2 + e \right) + \frac{\partial}{\partial x_\alpha} \left(\frac{1}{2} u^2 + e + \frac{p}{\rho} \right) \rho u_\alpha \\ &\quad = \frac{\partial}{\partial x_\alpha} \left(\kappa' \frac{\partial e}{\partial x_\alpha} \right) + \frac{\partial}{\partial x_\alpha} \left[\mu u_\beta \left(\frac{\partial u_\alpha}{\partial x_\beta} + \frac{\partial u_\beta}{\partial x_\alpha} \right) \right] + \frac{\partial}{\partial x_\alpha} \left(\lambda u_\alpha \frac{\partial u_\beta}{\partial x_\beta} \right) \end{aligned} \tag{22}$$

The pressure, the second viscosity, the conductivity of internal energy and the speed of sound are given, respectively, by

$$p = \frac{2}{D} \rho e \tag{23}$$

$$\lambda = -\frac{4}{D^2} \rho e (\phi - A) \tag{24}$$

$$\kappa' = \frac{2(D+2)}{D^2} \rho e (\phi - A) \tag{25}$$

and

$$a_{\mathrm{s}} = \sqrt{\frac{2(D+2)}{D^2} e} \tag{26}$$

DOI: 10.1002/fld

3. NUMERICAL ACCURACY

This section discusses the calculation speed-up, which becomes possible by modifying the relationship between the viscosity coefficient v and single relaxation coefficient ϕ by adding the term in Equation (15). To begin with, when the high Reynolds number is considered, it is the major difference between the modified FDLBM model and the conventional FDLBM model in Equation (1) that as $Re \to \infty$ the relaxation time $\phi \to 0.0$ in the conventional FDLBM, whereas $\phi \to A$ in the modified model. From this fact, the calculation stability to satisfy the condition $\Delta t/\phi < 2.0$, which is a condition of the coefficient depending on the collision term, could not be achieved if $\Delta t \to 0$ is not given in the conventional FDLBM. In the modified FDLBM, however, the time becomes $\Delta t \to 2.0 \cdot A$. Therefore, we can easily promote the calculation stability in Δt to some extent in size.

To examine the validity of the modified FDLBM, we use both the conventional model and the modified model by considering the characteristics of the shock wave and the reflection wave. A conceptual scheme of a shock tube is shown in Figure 2. The shock tube is a device in which normal shock waves are generated by the rupture of a diaphragm initially separating a high-pressure chamber from the low-pressure chamber. Upon rupturing the diaphragm, a normal shock wave moves into the low-pressure side, with a series of expansion waves propagating into the high-pressure side. The speed of shock c_s is defined as $c_s = M_s a_{sf}$, where M_s is the shock Mach number. The fundamental equation of shock tube can be written as

$$\frac{p_4}{p_1} = \frac{p_2}{p_1}\left[1 - \frac{(\gamma_4 - 1)(a_{sf}/a_{sr})(p_2/p_1)}{\sqrt{2\gamma_1}\sqrt{2\gamma_1 + (\gamma_1 + 1)(p_2/p_1 - 1)}}\right]^{-2\gamma_4/(\gamma_4 - 1)} \tag{27}$$

where a_{sf}, a_{sr} are the front and rear sound velocity of shock wave, respectively.

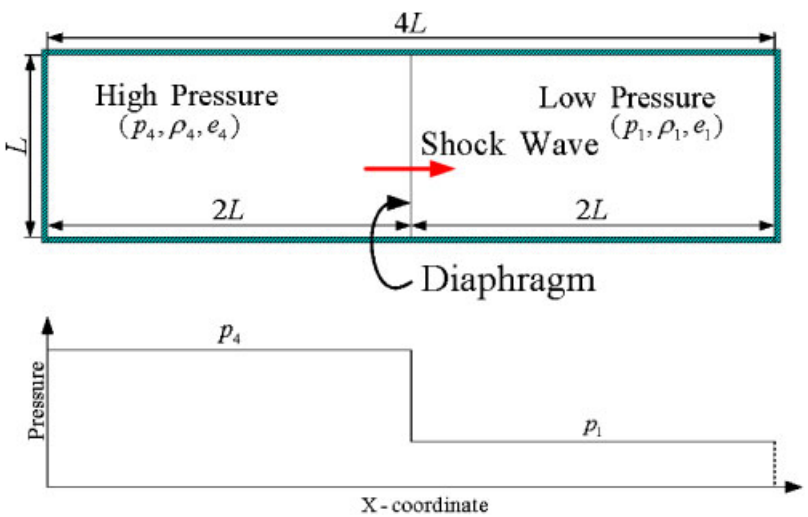

Figure 2. Simulated flow field in a shock tube.

DOI: 10.1002/fld

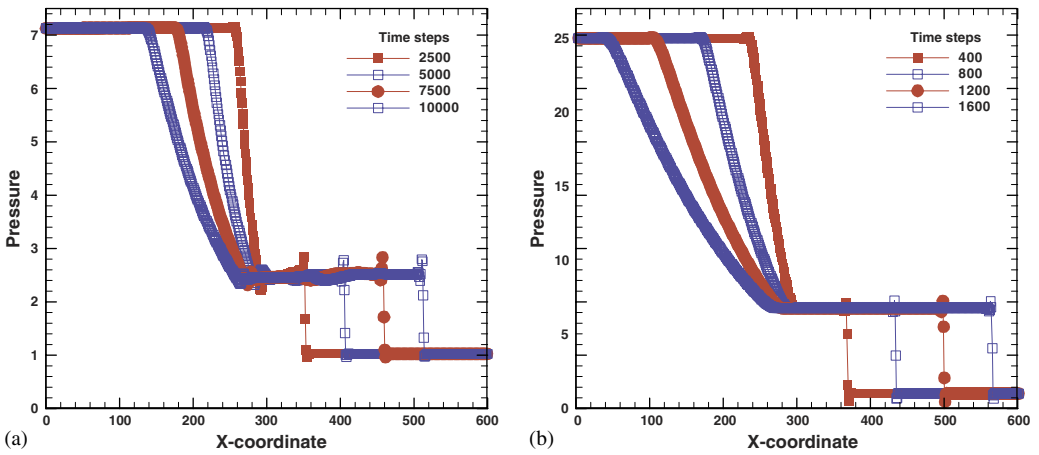

Figure 3. (a) Flow field in a shock tube simulated with D2Q21 model by the conventional FDLBM; and (b) the modified FDLBM.

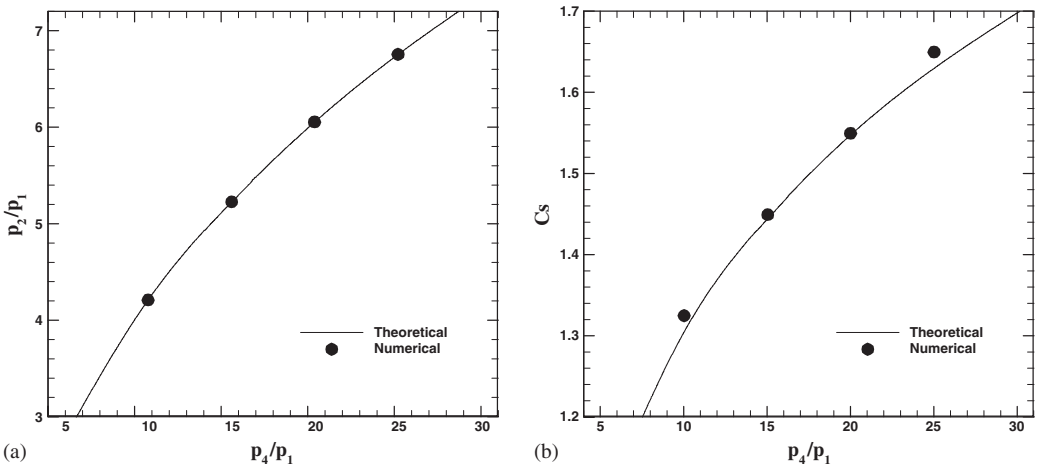

Figure 4. (a) Comparisons of the pressures at the front and rear of shock wave; and (b) the speed of shock with theoretical prediction by the modified FDLBM.

As for the initial parameters, if we set the initial pressure ratio in $p_4/p_1 = 7.0$, the time increment $\Delta t = 0.01$ and the internal energy in both partitions $e_1 = e_4 = 0.85$, the shock Mach number becomes $M_s = 1.645$. The simulated pressure distributions after the diaphragm are shown in Figure 3(a). It should be noted that the pressure ratio over 7.0 is not completed by applying the conventional FDLB model while, in the case of the modified model in Equation (15), we put the initial pressure ratio in $p_4/p_1 = 25.0$, the time $\Delta t = 0.1$ as the initial conditions, and the shock Mach number is $M_s = 2.215$. The simulated flow fields are shown in Figure 3(b). Here, it is certainly noted that the calculation with the modified model is stably completed even for the pressure ratios p_4/p_1 three

DOI: 10.1002/fld

times as high as those in the cases of the conventional model. Furthermore, in the cases shown in Figures 3(a) and (b), the modified model is capable of speeding up the calculation time over 10 times faster than that of the conventional model.

Figure 4(a) shows the relation between the initial pressure ratio and the pressure ratio of the front and the behind of shock wave. In this case, we estimate the error is within 0.02% and the results also agree well with the theoretical predictions. Figure 4(b) shows that the difference between the theoretical shock speed and the calculated shock speed is within 1.24%.

4. NUMERICAL RESULTS AND DISCUSSION

4.1. Aeolian tone

A dipole sound from a flow around a circular cylinder in a 2D uniform flow by Karman vortex shedding is considered for validation of the modified finite difference-based lattice Boltzmann model in Equation (15) described in Section 2. A schematic diagram of the uniform flow of the velocity U_0 in the x direction of Cartesian coordinates (x, y) and a circular cylinder are shown in Figure 5(a). Normalized by the static sound velocity a_0, the streamwise velocity is prescribed by the $M = U_0/a_0 = U_0/\sqrt{2e}$, where M is the Mach number. Furthermore, the cylinder of the diameter d is fixed at the origin. The polar coordinates (r, θ) are also used, where the azimuthal angle θ is defined from downstream in the counterclockwise direction. The Reynolds number, defined as $Re = U_0 d/\nu$, where ν is the kinematic viscosity, is equal to 150. In this study, solutions will be directly be compared for $Re = 150$ with that of DNS. That is, the two-dimensional aeroacoustic DNS results of the unsteady flow around a circular cylinder in a uniform cross-flow at $Re = 150$ calculated by Inoue [9] is chosen as the benchmark for the validation, under the premise that the DNS result is accurate enough to simulate the physical phenomena.

For the entire field from near to far acoustic field, computations are carried out on a O-grid configuration shown in Figure 5(b), where only one-quarter of the mesh lines for the radial direction

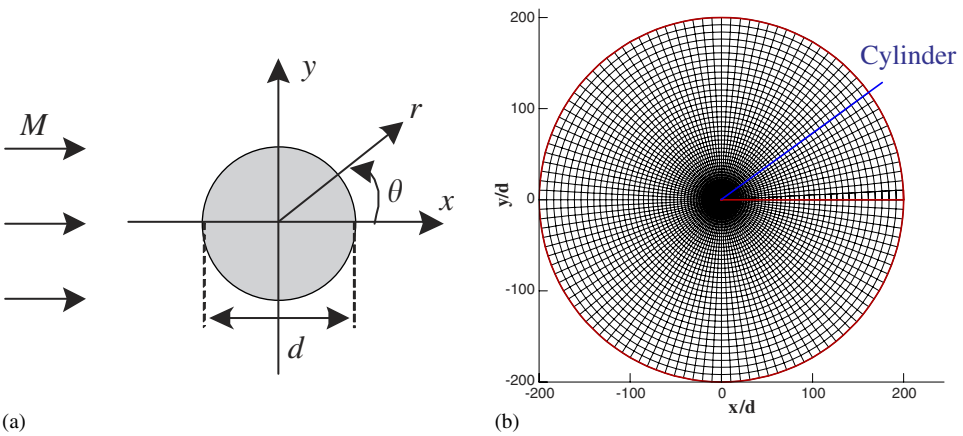

Figure 5. (a) Schematic diagram of the flow field model; and (b) computational mesh for flow past a circular cylinder. For clarity, only one in every four mesh lines for the radial direction is plotted.

DOI: 10.1002/fld

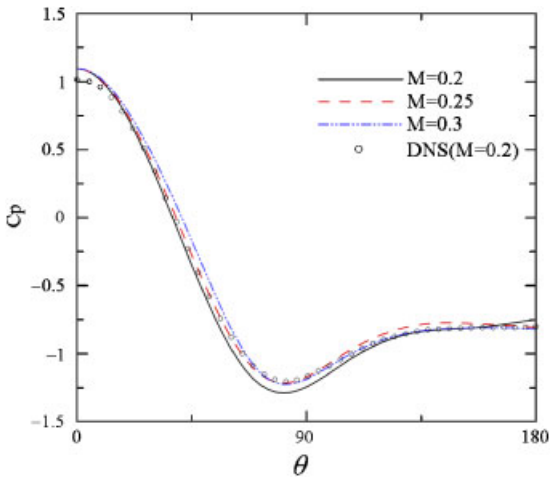

Figure 6. Time average pressure C_p at $M = 0.2$, 0.25, 0.3 and DNS result (Inoue, 2002) at $0 \leqslant \theta \leqslant \pi$. $Re = 150$.

are plotted for clarity. The computational domain is set to a circle of $r = 200d$ and is constructed as follows: the total number of the grid points is 24 321, 201 (r-direction) $\times$ 121 (θ-direction); the time increment Δt is 0.02; and the examined Mach numbers use the sound velocity by changing the internal energy e. All the calculations are in two-dimension and use D2Q21 model as shown in Figure 1. Computations start with uniform velocity $u_i(T(= Ut/d) = 0) = (U_0, 0)$ everywhere. For spatial derivatives, a third-order-accurate up-wind scheme (second-order-accurate at the boundary) is used, and a second-order-accurate Runge–Kutta scheme is used for time integration. Adiabatic and no-slip conditions are adopted on the cylinder surface. Along the O-grid shaped outer boundary whose radius is $r = 200d$, the velocities ($U_0 = 0.2$, 0.25 and 0.3) and internal energy $e_0 = 0.5$ are set at the freestream values, $u_i = (U_0, 0)$, therefore the Mach number correspond to $M = 0.2$, 0.25 and 0.3. Because the boundary is sufficiently far away from the circular cylinder, the numerical wave reflections from the boundary are removed [27]. The spacing in the surface region is prescribed to be fine enough to analyse the boundary layer on the cylinder surface. The acquired data is set forth sufficiently after the effect of the initial perturbation become negligible ($T \geqslant 100$).

Force acting on the cylinder surface as a function of the azimuthal angle θ is presented in Figure 6 for three different Mach numbers ($M = 0.2$, 0.25 and 0.3), and compared with that of DNS result [9]. Pressure coefficient C_p is the time averaged pressure on the cylinder surface normalized by the value at the stagnation point $\theta = 0°$, and defined as follows.

$$C_p = \frac{p - p_0}{1/2\rho_0 U^2} \tag{28}$$

Here, p_0 denotes the ambient pressure. From the figure, it shows that the coefficient C_p is not affected significantly by the Mach number. A comparison of the pressure coefficient at $0 \leqslant \theta \leqslant \pi$ for $M = 0.2$ also indicates that FDLBM is compatible with DNS.

In the near-field flow structure, lift force C_L acting on the cylinder surface and pressure variations are plotted in Figure 7 for the case of $M = 0.2$ ($e = 0.5$). Here, the sound pressure Δp is

DOI: 10.1002/fld

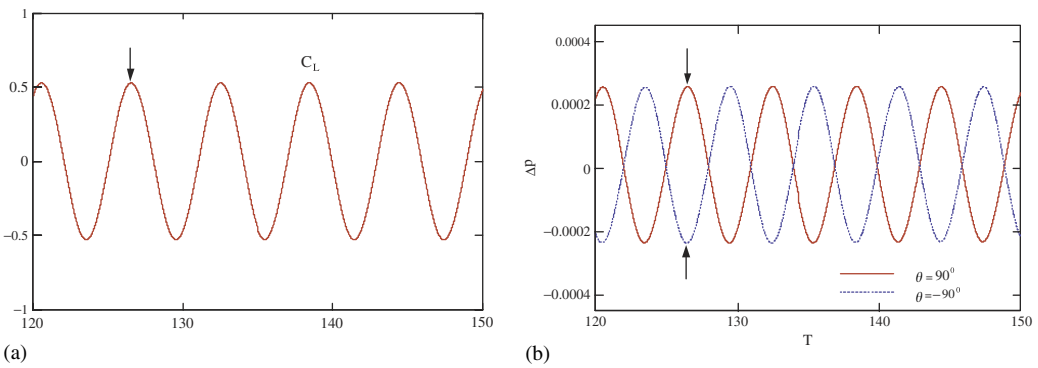

Figure 7. (a) Lift force acting on the cylinder surface; and (b) time history of the sound pressure. $M = 0.2$, $Re = 150$. Arrows indicate $T = 127$, $d = 50$; solid line $\theta = 90°$; dotted line $\theta = -90°$.

defined as

$$\Delta p = (p - p_0)/p_0 \tag{29}$$

The time history of sound pressure at the point $d = 50$ and $\theta = \pm 90°$ is shown in Figure 7(b). By comparing with the lift coefficient C_L in Figure 7(a), during the period $T (= Ut/d) = 120$–150, it can be seen that the period of C_L oscillates equal to the period of Δp. And positive peaks of C_L also coincide with the positive and negative peaks of $\Delta p_{\theta = \pm 90}$. In this case, the Strouhal number is defined by $S_t = fd/U$ where f is the frequency of the periodic vortex shedding. It is evaluated as $S_t = 0.177$, which is close to the experimental value (0.18 in Williamson) [28] and DNS result (0.183 in Inoue and Hatakeyama) [9].

Instantaneous distribution of the acoustic pressures measured at $\theta = 90°$ and the point $d = 100$ on the line perpendicular to the flow from the cylinder centre are given in Figure 8. In DNS by Inoue, the two-dimensional unsteady compressible Navier–Stokes equations were solved by a six-order-accurate compact Pade scheme for spatial derivatives and fourth-order Runge–Kutta scheme for time integration. The number of the grid is 438113, 871 (r-direction) $\times$ 503 (θ-direction). The Reynolds number is 150 and the Mach number is 0.2 for both cases. These two results are similar to them of Inoue and Hatakeyama [9]. However, such a DNS of aeroacoustic phenomena requires a large amount of computer resources, even though it is only two-dimensional. From Figures 7 and 8, this means that the current our simulation is much cheaper with respect to the computational costs than the acoustic of DNS, but it gives also a similar prediction to the DNS.

Figure 9 shows the acoustic pressure field at $T = 132$ for three different Mach numbers ($M = 0.2$, 0.25, and 0.3), where the contour level fluctuates at $\Delta p_{\text{step}} = 3 \times 10^{-4}$, 7.5×10^{-3} and 1.0×10^{-3}, respectively. The solid lines indicate the positive pressures and the dashed lines are the negative ones. As can be seen from this figure, rarefaction waves with negative Δp and compression waves with positive Δp are generated alternately around the cylinder at the origin, and propagate downstream and upstream, respectively.

Table I shows the difference between the theoretical prediction and the calculated value of the propagation speed. At all directions, the propagation speeds vary $a_\theta = a_s - U_0 \cos\theta$ by mean flow of the medium. In this case, the estimated error is within 2.1% and the results agree well with the theoretical predictions.

DOI: 10.1002/fld

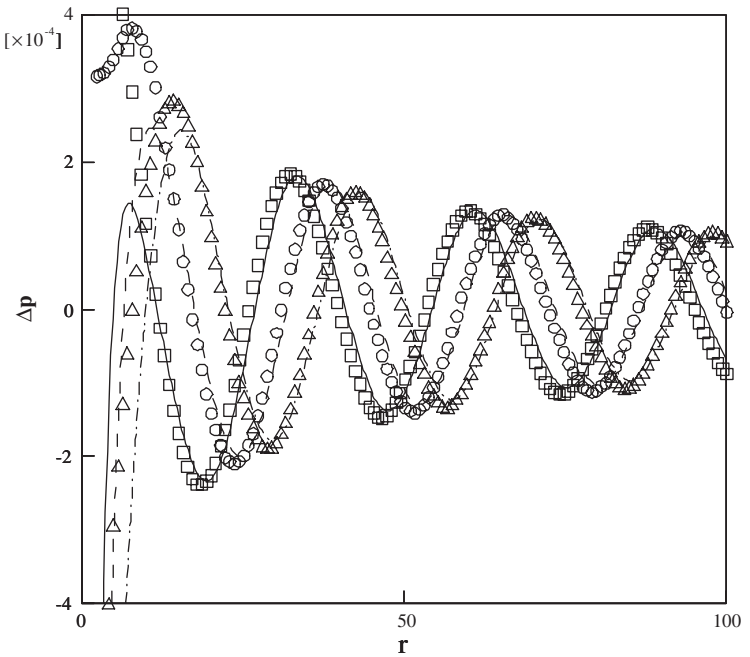

Figure 8. Comparison of pressure waves for FDLBM by third-order upwind and Navier–Stokes equation [9] at $M = 0.2$, $Re = 150$ and $\theta = 90°$. FDLBM: ———, $T = 130$; − − − −, $T = 131$; −·−·−, $T = 132$. N-S equation: □, $T = 2000$; ○, $T = 2005$; △, $T = 2010$.

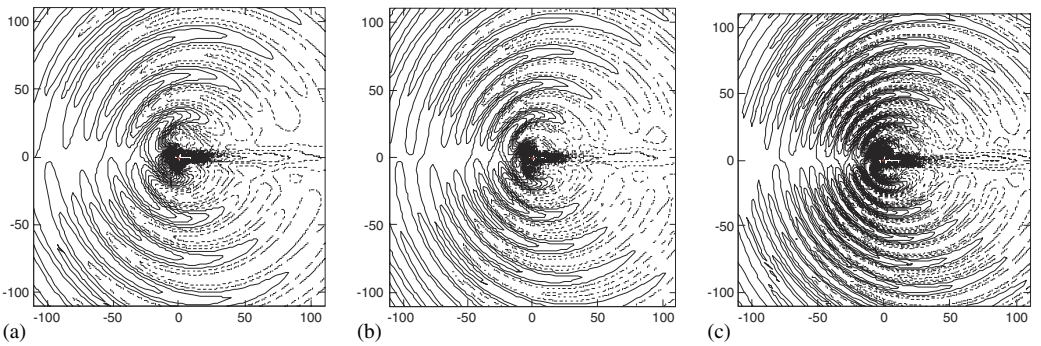

Figure 9. Contours of sound pressure at $T = 132$ and $Re = 150$ for three different Mach numbers. The contour level fluctuates at $\Delta p_{\text{step}} = 3 \times 10^{-4}$, 7.5×10^{-3}, and 1.0×10^{-3}, respectively. Solid lines: positive, dotted lines: negative: (a) $M = 0.2$; (b) $M = 0.25$; and (c) $M = 0.3$.

Figure 10 illustrates distributions and decays of the sound pressure plotted along the three different angles ($\theta = 45°$, 90° and 135°) for the case of $Re = 150$ and $M = 0.2$. The distributions of Δp are plotted against the radial distance r from the origin at the three different times $T = 130$, 131 and 132. Each peak of the waves is found to propagate and decay. The propagation speed of

DOI: 10.1002/fld

Table I. Numerical results of sound at each directon ($M = 0.2$).

θ	$\cos\theta$	$a'_\theta = a_\theta / U_0$	Δr	$\Delta r / a'_\theta$
45	0.707	4.293	4.277	0.996
90	0.0	5.00	4.891	0.978
135	−0.707	5.707	5.585	0.979

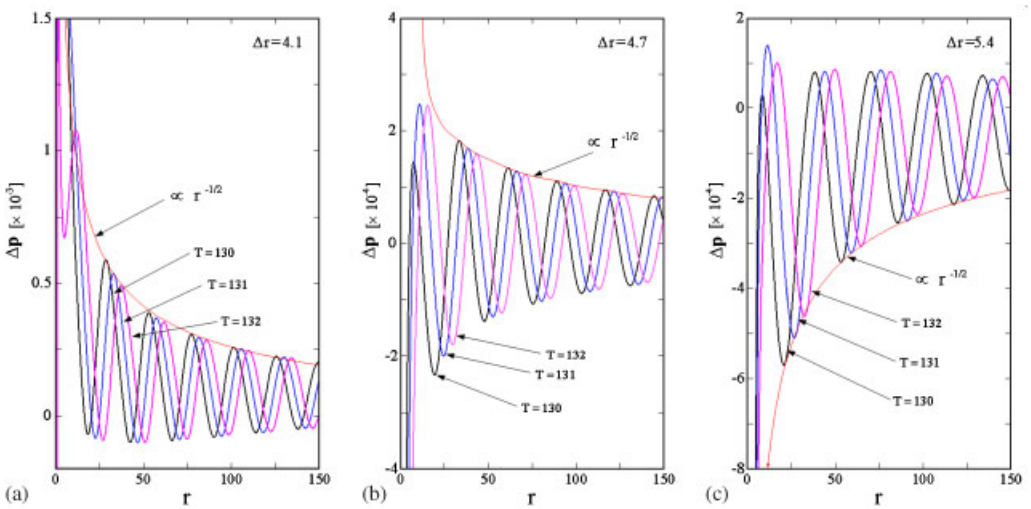

Figure 10. Distributions and decays of sound pressure at three different directions. $M = 0.2$. $Re = 150$: (a) $\theta = 45°$; (b) $\theta = 90°$; and (c) $\theta = 135°$.

the waves is equal to the speed of sound in the far field, in agreement with the linear acoustic theory. Also, the decaying curves are converged to the lines proportional to $r^{-1/2}$ in the far field, which is again in accordance with the theory. These results suggest that the sounds generated from the cylinder at low Reynolds numbers are precisely captured by FDLBM if both the flow dynamics in the near field and the wave propagations in the far field are computed with high accuracy.

Furthermore, to validate the lattice dependence, we consider the unsteady flowfield and the sound generated by a NACA0012 airfoil (see Figure 11) placed in a two-dimensional uniform flow. The number of the grid is 62 307, $301(x) \times 207(y)$. The computational domain is a rectangle ($-17L \leqslant x \leqslant 18L$ and $-17.5L \leqslant y \leqslant 17.5L$) of a block structured H-grid system, where L is the length of chord. x and y are the dimensionless coordinates nominated with the length of chord L and with the origin at the start of airfoil. The grid spacing in the x- and y-directions are nonuniform. The geometry of the computational domain and the coordinate system are shown in Figure 11. The initial conditions are set to $Re = 200$, $U_0 = 0.2$, $M = 0.2$ ($e = 0.5$) and an angle of attack is given $\alpha = 14°$. All calculation conditions are the same in the case of the circular cylinder. The solid lines indicate the positive pressures and the dashed lines are negative ones. As can be seen from Figure 12, rarefaction waves with negative Δp and compression waves with positive Δp are

DOI: 10.1002/fld

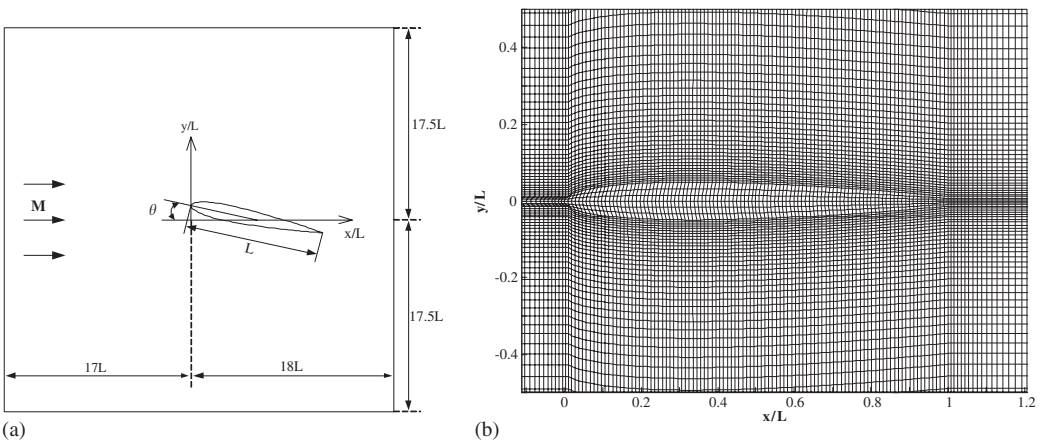

Figure 11. (a) Schematic diagram of the flow field; and (b) computational mesh with NACA0012 (enlarged).

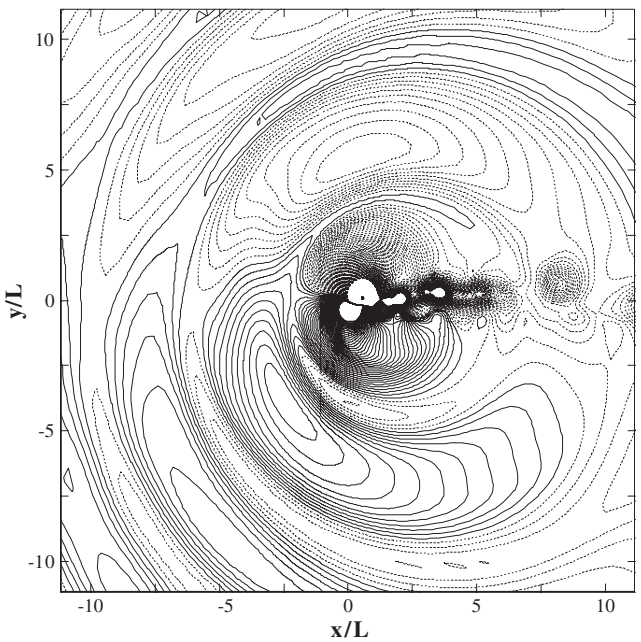

Figure 12. Contours of sound pressure past a NACA0012 airfoil at 14° angle of attack. $T = 156$, $Re = 200$ and $M = 0.2$.

generated alternately around the NACA0012 airfoil at the origin, and it propagate downstream and upstream, respectively. These results verify that the acoustic waves have an isotropic characteristic regardless of the lattice shapes.

DOI: 10.1002/fld

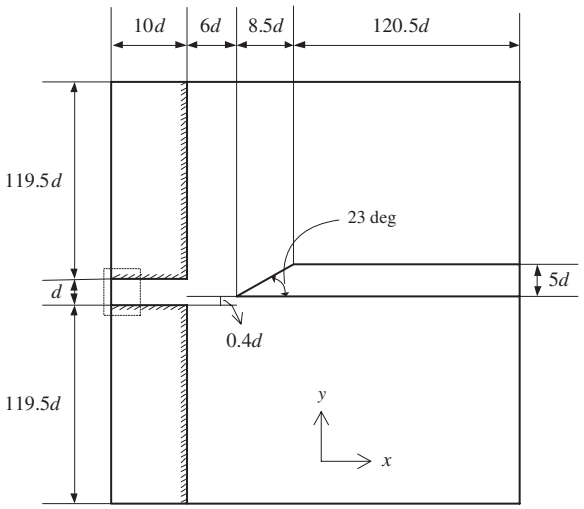

Figure 13. Edgetone geometry.

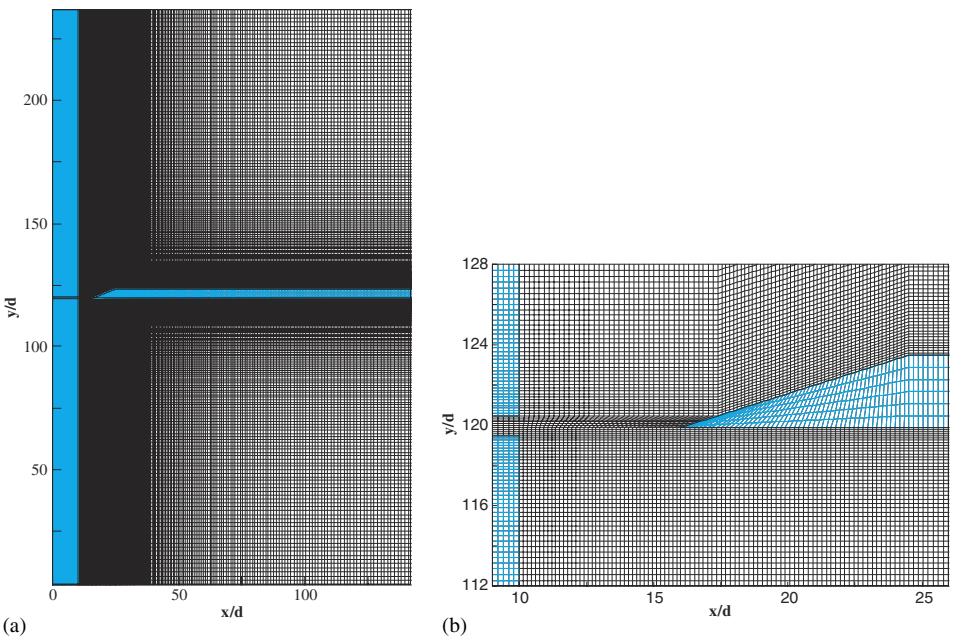

Figure 14. Computational grid for Edgetone of $Re = 1000$: (a) total mesh; and (b) mesh close to the edge.

4.2. Edge tone involving feedback

The calculation results at Mach number $M = 0.2$, $U_0 = 0.2$ and $Re = 1000$ are described as shown in Figures 13–20. The dimension of the edgetone is shown in Figure 13 and all the length scales

DOI: 10.1002/fld

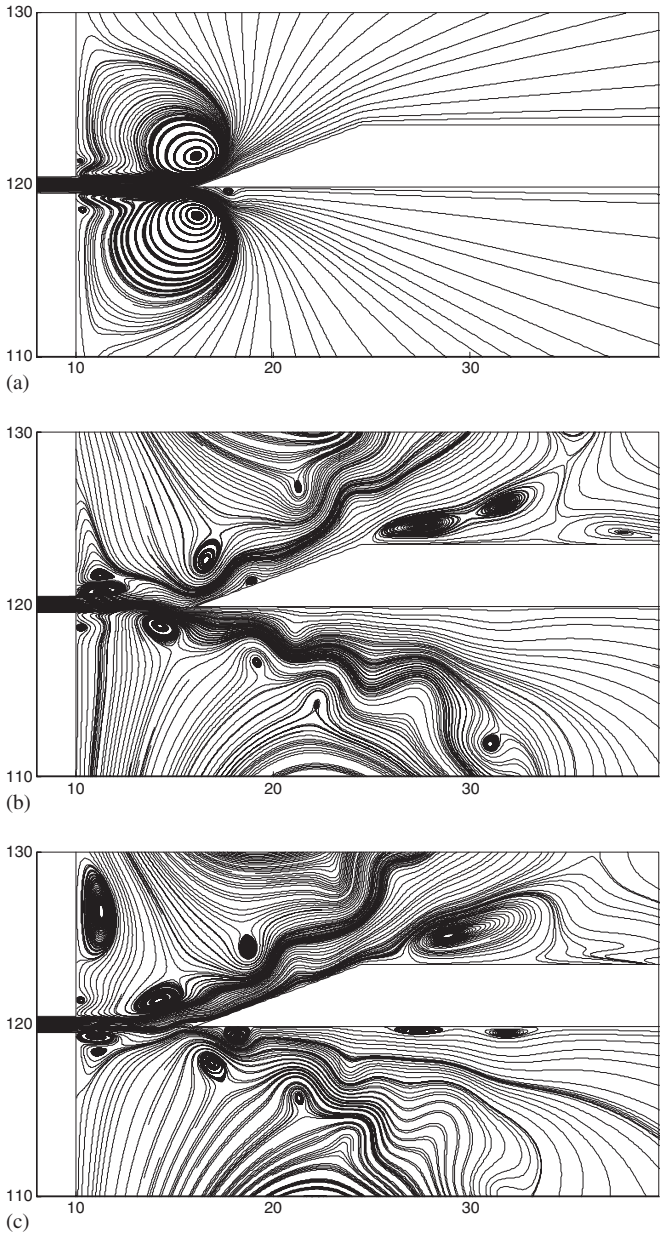

Figure 15. Streamlines at three different instants for $M = 0.2$, $U_0 = 0.2$ and $Re = 1000$: (a) $T(= Ut/d) = 20$; (b) $T(= Ut/d) = 260$; and (c) $T(= Ut/d) = 268$.

are normalized by the width of nozzle d in the computation. Flows are assumed to be laminar with the same incoming velocity. For the hydrodynamic and flow-induced noise calculations, a computational domain is set for $0 \leqslant x \leqslant 145d$ and $0 \leqslant y \leqslant 240d$ (301×301 mesh cells; see

DOI: 10.1002/fld

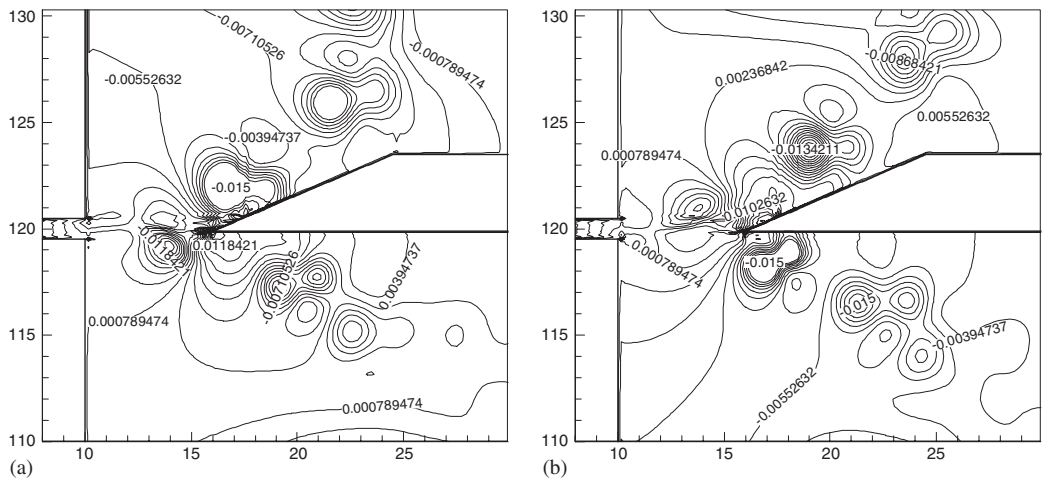

Figure 16. Pressure distribution at two different instants ($-0.015 \leqslant \Delta p \leqslant 0.015$): (a) $T(=Ut/d)=260$; and (b) $T(=Ut/d)=268$.

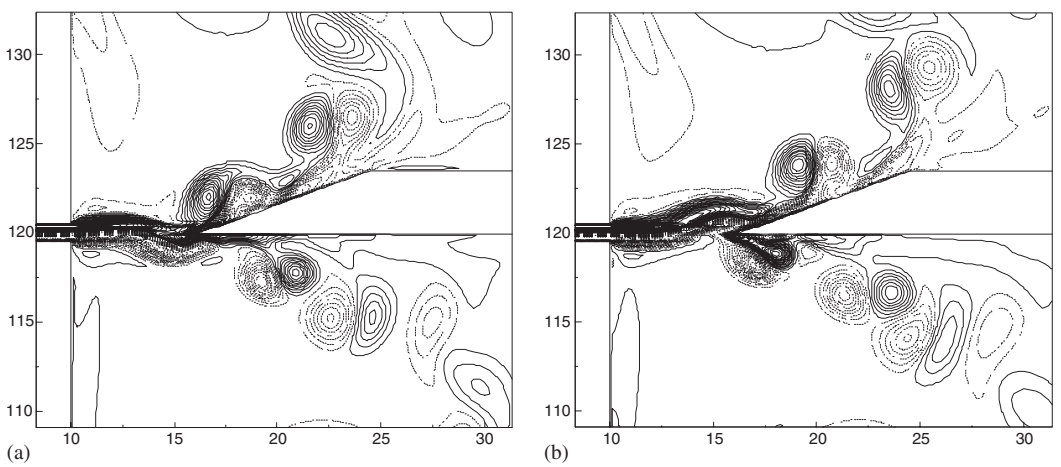

Figure 17. Instantaneous plots of a vorticity field: (a) $T(=Ut/d)=260$; and (b) $T(=Ut/d)=268$.

Figure 14). Adiabatic and no-slip conditions are employed on the wedge and walls, and an outflow condition is imposed on the outer far field boundary.

A jet which comes out of the nozzle first collides with the edge since a uniform flow as initial condition without a turbulence is given, and the jet equally divided itself into the upper and lower of the wedge as shown in Figure 15(a). Then, the jet begins to fluctuate, colliding with the edge. It fluctuates upward and downward periodically. This fluctuation synchronizes with the period of the vortex, which arises from the top and bottom wall in the vicinity of the nozzle exit. It is considered

DOI: 10.1002/fld

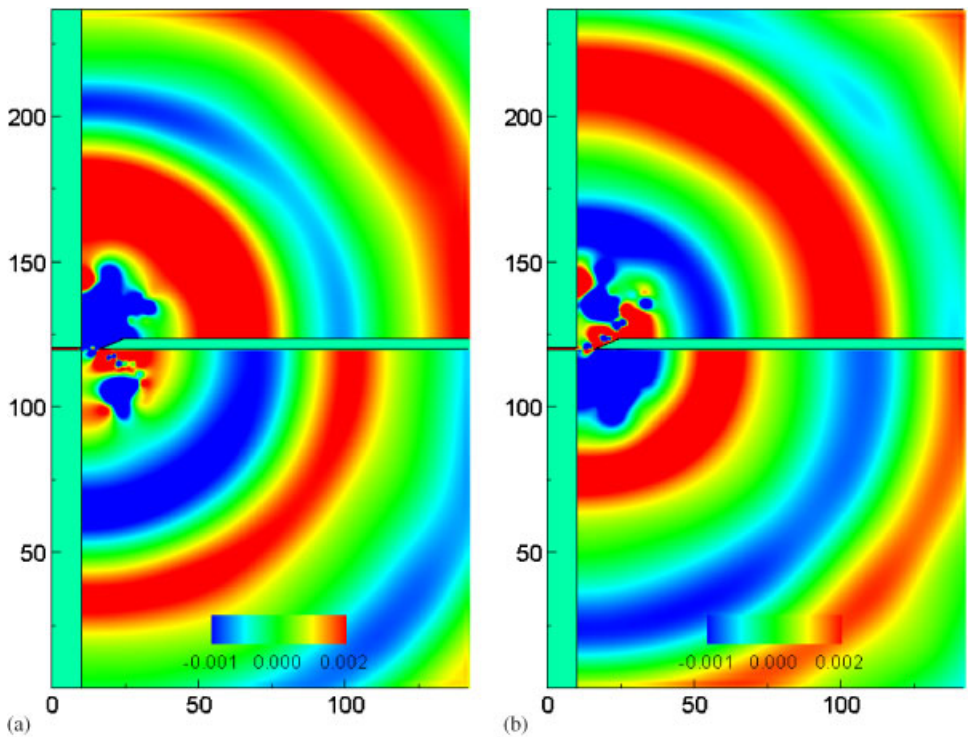

Figure 18. Acoustic pressure distribution ($-0.001 \leqslant \Delta p \leqslant 0.002$): (a) $T(=Ut/d)=260$; and (b) $T(=Ut/d)=268$.

that, because of the vortex, the fluctuation of the jet is induced. Then with the effect of jet, the vortex moves toward the downstream, and it undulates like the form of the jet by the rotation energy. As a result, the jet changes its direction due to the rotation of vortex in the vicinity where the vortex exceeded the tip of the wedge, and flows into a unilateral of the wedge, as shown in Figures 15(b) and (c). Owing to the fluctuation of this jet as shown in Figure 15, the pressure on the side exposing to the jet increases (Figure 16(b)) but, on the opposite side, the pressure decreases (Figure 16(a)) periodically. In other words, the edgetone is generated because the impinging jet forms a self-excited flow maintained by a feedback loop. As a result, on the upper and lower parts of the edge, the pressure wave with an opposite phase is generated. It is shown that the maximum pressure $p_{\max}$ and minimum pressure $p_{\min}$ have been observed to be $p_{\max}=0.0345$ and $p_{\min}=-0.0289$, respectively, at the vicinity of the edge as has been examined by Kayayoglu and Rockwell [29]. This feature is to be explained by the antisymmetry of the downstream disturbance about the central surface of jet.

Vortices in the jet impinge on to the surface of the wedge to produce a surface-pressure fluctuation which propagates upstream at the speed of sound to the nozzle. At the outlet of the nozzle, this pressure fluctuation produces vorticity fluctuation in the shear layers of the jet, modifying the rolling up of the shear layers due to the instability. Figure 17 shows instantaneous plots of a vorticity field. During the two periods, edge vortices are observed above and below the edge, being

DOI: 10.1002/fld

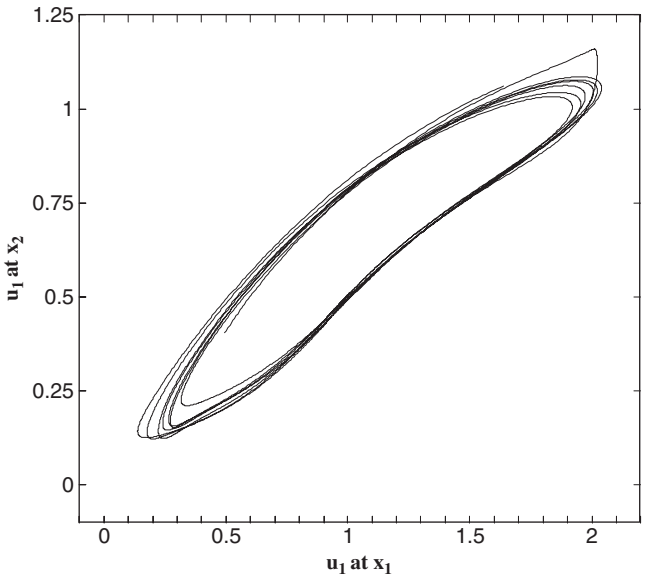

Figure 19. Phase diagram at two different positions.

180° out of phase to each other. In the figures, the vortex is below the edge during the downward movement of the jet. In other words, the vortices in the shear layer impinge on the downstream edge and induce large pressure oscillations, which become the major noise sources. At certain conditions periodic movement due to positive feedback mechanism occurs, and it creates audible acoustic pressure. In addition, since the sound radiation by the edge is proportional to the surface pressure, the maximum pressure point can be regarded as the effective source point, though the exact point can be somewhat different depending on the radiating direction.

Figure 18 shows the acoustic pressure field for two different instants ($T = Ut/d = 260$ and 268), where the contour level Δp_{step} fluctuates from -0.001 to 0.003. We can see in the figure that the acoustic pressure of positive and negative propagates symmetrically in the upper and lower parts of the wedge alternately. Figure 19 shows a phase diagram $u_1(x_2, 0.6d)$ versus $u_1(x_1, 0.6d)$ with x_2 a point $w/5$ left of x_1. Here, we analysed the temporal behaviour of a typical quantity of the flow at a fixed position x_1 after computing for a sufficiently large number of periods. Here, we used x_1, a point $w/5$ left and slightly above the edge of the labium. For quantity we chose the horizontal velocity component $u_1(x_1, 0.6d)$ at x_1, and it demonstrates the periodic behaviour of the flow.

The time variations of the acoustic pressure at 6 points in calculating area are shown in Figure 20. The observation points are radically considered on the edge tip, in which these points apart from $(109d, \pm 100d)$, $(109d, \pm 20d)$ and $(0d, \pm 100d)$ in the x- and y-direction, respectively. The solid line is the upper side of the wedge, and the dotted one is the lower side of the wedge, and the sound signals fluctuate with a period of $\Delta T(= Ut/d) = 16.51$, which corresponds to $S_t(= fd/U) = 0.061$. Moreover, it can be confirmed that the amplitude of the fluctuations of the acoustic pressure in the points is about 0.0025, and it has a more minute value than the pressure fluctuation at the vicinity of the edge with 0.01.

DOI: 10.1002/fld

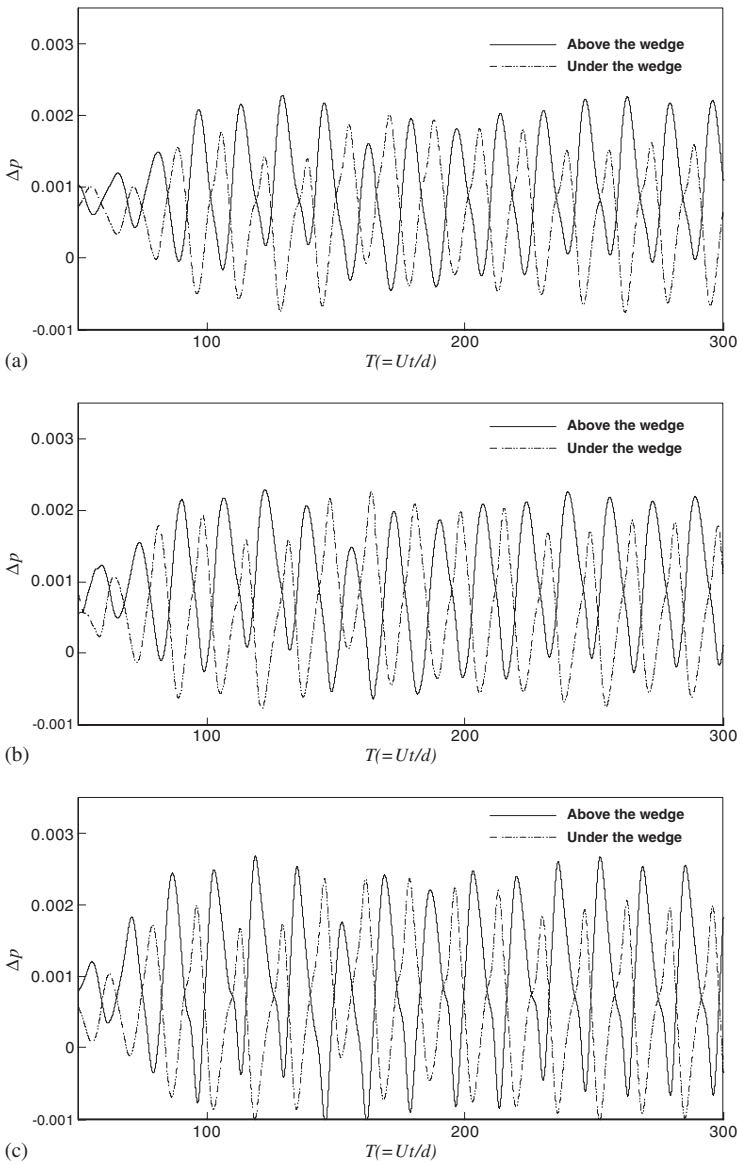

Figure 20. Time variation of acoustic pressure at three different positions: (a) A1($109d, \pm 100d$); (b) A2($109d, \pm 20d$); and (c) A3($0d, \pm 100d$).

5. CONCLUSIONS

The use of a modified FDLB model of two-dimensional 21 velocity for simulating flow noise is considered. The modified FDLB model demonstrated that the calculation in shock tube is stably

DOI: 10.1002/fld

completed even for the pressure ratio p_4/p_1 three times as high as those in the case of the conventional model of Equation (1). Furthermore, the modified model is capable of speeding up the simulation time over 10 times faster than that of the conventional model.

The flow-induced noise of self-sustained oscillatory flow at low Mach number was simulated by using the modified FDLB model with the third-order-accurate up-wind scheme and the second-order-accurate up-wind Runge–Kutta method. The sound frequency was the same as the vortex shedding frequency of the Karman vortex street. The rarefaction waves and the compression waves were alternately generated and propagated in the directions perpendicular to the uniform flow. The sound pressure also decayed proportional to $r^{-1/2}$ in the far acoustic field, which agreed with the theoretical prediction. The analysis with the square cylinder and NACA0012 also elucidated that the acoustic waves have an isotropic characteristic regardless of the lattice shapes.

The present method correctly predicted the frequency characteristics of the discrete oscillations of a jet-edge feedback cycle at $Re = 1000$ and $M = 0.1$–0.3. We successfully captured small pressure fluctuations resulting from periodically oscillation of jet around the edge with angle of $\alpha = 23°$.

ACKNOWLEDGEMENTS

This work was supported by Korea Research Foundation Grant funded by the Korea Government (MOEHRD, Basic Research Promotion Fund) (KRF-2005-050-D00002).

REFERENCES

1. Williamson CHK. Vortex dynamics in the cylinder wake *Annual Review of Fluid Mechanics* 1996; **28**:477–539.
2. Persillon H, Braza M. Physical analysis of the transition to turbulence in the wake of a circular cylinder by three-dimensional Navier–Stokes simulation. *Journal of Fluid Mechanics* 1998; **365**:23–88.
3. Wang M, Lele SK, Moin P. Computation of quadrupole noise using acoustic analogy. *AIAA Journal* 1996; **34**(11):2247–2254.
4. Curle N. The influence of solid boundaries upon aerodynamic sound. *Proceedings of the Royal Society of London, Series A* 1955; **231**:505–514.
5. Hardin JC, Lamkin SL. Aeroacoustic computation of cylinder wake flow. *AIAA Journal* 1984; **22**:51–57.
6. Shen WZ, Sorensen JN. Comment on the aeroacoustic formulation of Hardin and Pope. *AIAA Journal* 1999; **37**:141–143.
7. Slimon SA, Soteriou MC, Davis DW. Computational aeroacoustics simulations using the expansion about incompressible flow approach. *AIAA Journal* 1999; **37**:409–416.
8. Colonius T, Lele SK, Moin P. Sound generation in a mixing layer. *Journal of Fluid Mechanics* 1997; **330**:375–409.
9. Inoue O, Hatakeyama N. Sound generation by a two-dimensional circular cylinder in a uniform flow. *Journal of Fluid Mechanics* 2002; **471**:285–314.
10. Powell A. On the edge tone and associated phenomena. *Acoustica 3* 1953; **3**:233–243.
11. Powell A. On the edge tone. *Journal of Acoustical Society of America* 1961; **33**:395–409.
12. Brown GB. The vortex motion causing edge tones. *Proceedings of the Physical Society* 1937; **49**:493–507.
13. Holger DK, Wilson TA, Beavers GS. Fluid mechanics of the edgetone. *Journal of Acoustical Society of America* 1977; **62**(5):1116–1128.
14. Crighton DG. The jet edge-tone feedback cycle; linear theory for the operating stages. *Journal of Fluid Mechanics* 1992; **234**:361–391.
15. Ohring S. Calculations pertaining to the dipole nature of the edge tone. *Journal of Acoustical Society of America* 1988; **83**:2047–2085.
16. Bernard PS. Turbulence effects in the edgetone flow fields. *Journal of Fluids and Structures* 1990; **4**:449–470.
17. Park JH, Lee DJ. Numerical simulation of vortex-wedge interaction. *AIAA Journal* 1994; **32**:1126–1134.
18. Buick JM, Buckley CL, Greated CA, Gilbert J. Lattice Boltzmann BGK simulation of nonlinear sound waves: the development of a shock front. *Journal of Physics A: Mathematical and General* 2000; **33**:3917–3928.

DOI: 10.1002/fld

19. Tsutahara M, Kurita M, Kataoka T. Direct simulation of acoustic waves by the finite difference lattice Boltzmann method. *Transaction of JSME*, *Series B* 2003; **69**(680):841–847.
20. Chopard B, Droz M. *Cellular Automata Modeling of Physical Systems*. Cambridge University Press: Cambridge, MA, 1998.
21. Alexander FJ, Chen S, Sterling DJ. Lattice Boltzmann thermodynamics. *Physical Review E* 1993; **47**:2249–2252.
22. Chen Y, Doolen GD. Lattice Boltzmann method for fluid flows. *Annual Review of Fluid Mechanics* 1998; **30**:329–364.
23. Yu H, Zhao K. Lattice Boltzmann method for compressible flows with high Mach numbers. *Physical Review E* 2000; **61**(4):3867–3870.
24. Cao N, Chen S, Jin S, Martinez D. Physical symmetry and lattice symmetry in the lattice Boltzmann method. *Physical Review E* 1997; **55**:R21–R24.
25. Kang HK, Tsutahara M, Ro KD, Lee YH. Numerical simulation of shock wave propagation using the finite difference lattice Boltzmann method. *KSME International Journal* 2002; **16**(10):1327–1335.
26. Mei R, Shyy W. On the finite difference-based lattice Boltzmann method in curvilinear coordinates. *Journal of Computational Physics* 1998; **143**:426–448.
27. Pointsot T, Lele SK. Boundary conditions for direct simulation of compressible viscous flows. *Journal of Computational Physics* 1992; **101**:104–129.
28. Williamson CHK. Oblique and parallel modes of vortex shedding in the wake of a circular cylinder at low Reynolds numbers. *Journal of Fluid Mechanics* 1989; **206**:579–627.
29. Kaykayoglu R, Rockwell D. Unstable jet-edge interaction. Part 1. Instantaneous pressure fields at a single frequency. *Journal of Fluid Mechanics* 1986; **169**:125–149.

DOI: 10.1002/fld